# Dipole-exchange spin waves in magnetic thin films at zero and finite temperature: Theory and simulations

E. Meloche,[1] J. I. Mercer,[2] J. P. Whitehead,[2,*] T. M. Nguyen,[2] and M. L. Plumer[2]
[1]*Seagate Technology, One Disc Drive, Bloomington, Minnesota 55435, USA*
[2]*Department of Physics and Physical Oceanography, Memorial University, St. John's, NL, Canada A1B 3X7*
(Received 5 November 2010; revised manuscript received 29 January 2011; published 11 May 2011)

The excitation spectra in a stacked square lattice of dipole-exchange coupled classical spins is studied using both standard linearized spin-wave theory and the direct integration of the torque equation. A detailed comparison of the two methods is presented for the case of small-amplitude spin-wave modes. The spin-wave frequencies obtained from the time-dependent correlation functions calculated by integrating the equation of motion are shown to be in excellent agreement with the results obtained from linearized spin-wave theory for both single-layer and multilayer films. Applying the numerical integration method, the finite-temperature correlation function is calculated using Monte Carlo spin dynamics for the case of a single-layer, dipole-exchange coupled system. Values for the frequencies, amplitudes, and decay constant of the spin-wave modes at finite temperature are calculated from a spectral analysis of the finite-temperature correlation function. It is shown that thermal fluctuations give rise to a softening of the spin-wave frequencies and an intrinsic damping of the spin-wave oscillations.

DOI: 10.1103/PhysRevB.83.174425 PACS number(s): 07.05.Tp, 75.30.Ds, 75.70.−i, 75.10.Hk

## I. INTRODUCTION

The dynamical properties of magnetic thin films have attracted increasing interest recently as a means to probe fundamental aspects of magnetic interactions and their interplay with geometrical effects, and also because they provide the foundations for promising applications in spintronics and data storage.[1–5] Spin waves contribute significantly to the thermal noise in magnetic sensors,[6] and opportunities for noise reduction through design engineering can be enhanced through further understanding of magnetic excitations. The calculation of spin-wave dynamics in constrained geometries, such as magnetic thin films, is complicated by dipolar interactions, which can play a significant role in determining both the nature of the equilibrium spin configuration[7,8] as well as the dynamics.[9–13] The anisotropic and long-range character of the dipole interaction introduces a substantial level of complexity into both theoretical and numerical calculations and can combine with the typically stronger but more localized exchange interaction to generate equilibrium, inhomogeneous spin structures, and nontrivial excitations.

The significance of the dipolar interactions in determining the dynamical properties of magnetic thin films was illustrated in an early paper by Damon and Eshbach,[9] who calculated the characteristic modes of a magnetic thin film in the magnetostatic limit and found that the nature of the modes changes from bulk to surface with increasing frequency. These surface excitations are typically referred to as Damon-Eshbach (DE) modes. Later work by Benson and Mills[10] examined the case of a dipole-exchange system consisting of a stacked square lattice, which included both the dipole and exchange interactions. Solving the linearized equation of motion for the system, they obtained the eigenvalue solutions corresponding to the spin-wave modes for 50–100 layers. From the form of the eigenvectors, they were able to identify both surface and bulk modes. However, Benson and Mills were unable to find any evidence of the magnetostatic modes predicted by Damon and Eshbach. This apparent discrepancy between the predictions of Damon and Eshbach and the lattice model calculations of Benson and Mills were addressed in the later work of Erickson and Mills.[12] Extending the earlier work of Benson and Mills, their calculations revealed a crossover from a single DE-like surface mode at long wavelength to a pair of exchange-dominated surface modes as the wave number increased. In particular, they were able to show that, due to the effects of the exchange interaction, the frequency of the DE surface mode fell below the bulk modes for $q = 0$, but rose rapidly with increasing wave vector, mixing strongly with the bulk modes to form a band of exchange-dominated bulk modes and two surface modes at large wave number. The results of the Benson and Mills calculations were also shown to be in good agreement with earlier Brillouin scattering experiments on ultrathin magnetic layers composed of a only a few atomic layers.[14]

The formalism developed by Benson and Mills has been extended to more complex structures, including nanospheres,[15] nanowires,[16] and stripes,[17] and it has been applied with some success in analyzing and interpreting spectra obtained from Brillouin scattering experiments.[18,19] However, subsequent theoretical calculations of spin-wave spectra in constrained geometries have largely been limited to zero or low temperature and in highly symmetric systems,[20] or they have not included dipole effects at finite temperature.[21] An alternative approach to calculating spin-wave spectra at finite temperature is Monte Carlo spin dynamics, which combines the numerical integration of the equations of motion with initial states generated from Monte Carlo simulations. This technique has been used extensively to study the finite-temperature spin dynamics in a variety of two-[22–26] and three-dimensional[27–30] systems. The results obtained from Monte Carlo spin dynamics compares well with both experimental and theoretical results.[26,30,31] A key feature of Monte Carlo spin dynamics is that it requires averaging over a large number of trajectories generated from an ensemble of initial states. Thus while the method is computationally very demanding, it is capable of producing

 

reliable results to a high degree of precision for complex systems that are not predicated on the assumptions that limit the range and applicability of many theoretical approaches. Monte Carlo spin dynamics also serves as a useful bridge between the atomistic models of magnetic systems and the more phenomenological micromagnetics[32] approach that is used extensively to study problems in magnetism that are of a more applied nature, a distinction that becomes more blurred with the increasing importance of nanotechnology in magnetic device applications.

In this paper, we study the spin-wave excitations in magnetic thin films by numerically integrating the equations of motion for a two-dimensional system of dipole-exchange coupled classical spins in an applied external field aligned parallel to the plane of the film. Results are presented for both zero temperature and finite temperature using Monte Carlo spin dynamics. The paper consists of three main parts. In Sec. II A, a detailed formulation of linear spin-wave theory is presented and the form of the dynamic spin-spin correlation function for a two-dimensional system of dipole-exchange spins is calculated for small-amplitude spin-wave oscillations. The specific form of the dynamic spin-spin correlation function is key to properly identifying and calculating the properties of the finite-temperature spin waves from Monte Carlo spin dynamics. In Sec. II B, we compare the spin-wave spectra calculated from the linear spin-wave theory using the formalism developed in Sec. II A with the results obtained by numerical integration of the equations of motion. Results obtained for the single-layer and five-layer cases using both methods are presented for both dipole and dipole-exchange coupled systems and are shown to be in very good agreement. In Sec. III, the numerical integration technique used in Sec. II B is combined with the results from Monte Carlo simulations to compute the finite-temperature dynamic correlation function using Monte Carlo spin dynamics. Based on the form of the correlation function calculated in Sec. II A, the frequency, decay constant, and amplitude of the finite-temperature spin-wave modes are calculated. Results are presented for several wave numbers and temperatures. We close the paper with a discussion of the results. It is important to note that the calculations described in the present work do not include any explicit damping, and that the decay in the spin-wave modes observed in the finite-temperature results arises entirely as a result of the thermal fluctuations.

## II. SMALL-AMPLITUDE SPIN WAVES IN FERROMAGNETIC FILMS

In this section, we compare the properties of small-amplitude spin-wave oscillations for a stacked two-dimensional square lattice of dipole-exchange coupled classical spins calculated by two methods: linearized spin-wave theory and numerical integration of the equation of motion. The principal purpose of this section is to demonstrate that, with sufficient care, it is possible to obtain results from both methods that are in very good agreement. This work also serves as an important prelude to the finite-temperature results obtained using Monte Carlo spin dynamics that are presented in the following section, as well as more complicated systems that cannot be easily treated analytically, even in the small-amplitude approximation.

We consider a model system composed of $L$ square lattices with lattice constant $a$, stacked so that the vertices in adjacent layers are aligned along a common axis, perpendicular to the plane of the film. For simplicity, we consider the spacing between layers to be equal to the lattice constant $a$. A classical spin vector of magnitude $S$ is located at each of the vertices with a uniform field of magnitude $H$ applied along one of the lattice axes. The coordinates are defined such that $x$ and $z$ lie in the plane along the axes of the lattice, with the $z$ axis directed along the direction of the applied field. The coordinate $y$ is perpendicular to the plane. The specifics of the model are then defined in terms of the energy for a particular spin configuration, which is given by

$$\mathcal{E} = -h\sum_i S_i^z - \sum_{\langle ij\rangle} J_{ij}\vec{S}_i\cdot\vec{S}_j + \frac{1}{2}g\sum_{i\neq j}\sum_{\alpha,\beta} D_{ij}^{\alpha\beta}S_i^\alpha S_j^\beta. \tag{1}$$

Here $J_{ij}$ is the exchange coupling between sites $i$ and $j$, and $h = g_L\mu_B H$ represents the field applied along the $z$ axis. The last term in Eq. (1) represents the long-range dipole-dipole interactions with the dipolar tensor defined as

$$D_{ij}^{\alpha\beta} = \frac{|R_{ij}|^2\delta_{\alpha\beta} - 3R_{ij}^\alpha R_{ij}^\beta}{|R_{ij}|^5}, \tag{2}$$

where $\alpha,\beta = x,y,z$, $\vec{R}_{ij} = (\vec{r}_j - \vec{r}_i)/a$ is a vector joining sites $i$ and $j$ measured in units of the lattice constant $a$, and $g = g_L^2\mu_B^2/a^3$, where $g_L$ is the Landé factor and $\mu_B$ is the Bohr magneton. The model can be readily generalized to consider other lattice structures and geometries, including simple antiferromagnetic structures,[33,34] as well as other types of anisotropic interactions, such as axial anisotropy, anisotropic exchange, and the Dzyaloshinkii-Moryia interaction.

Within the classical formalism, the evolution of the spin vectors may be calculated from the torque equation given by

$$\frac{d\vec{S}_i}{dt} = -\vec{S}_i\times\vec{h}_i, \tag{3}$$

where the effective field $\vec{h}_i$ is defined from the expression for energy given in Eq. (1) as

$$h_i^\alpha = -\frac{\partial\mathcal{E}}{\partial S_i^\alpha} = h\delta_{z\alpha} + \sum_j J_{ij}S_j^\alpha - g\sum_{j\neq i} D_{ij}^{\alpha\beta}S_j^\beta. \tag{4}$$

These classical equations of motion reproduce results from a quantum-mechanical formalism, based on the operator equation of motion, in the case of large spin number $S$.[35]

### A. Linearized spin-wave theory

In this model, we assume that the applied field is sufficiently strong such that the spins are ferromagnetically aligned in the direction of the field. For the case of small-amplitude oscillations, we may therefore assume that $S_j^z \approx S$ and that $S_j^x \ll S$ and $S_j^y \ll S$. Retaining only the terms linear in the transverse spin components in the equation of motion defined

by Eqs. (3) and (4), we obtain the linearized equations of motion,

$$\frac{d}{dt}S_j^x = -h_0 S_j^y - S\sum_i \left(J_{ij} - gD_{ij}^{yy}\right)S_i^y + gS\sum_i D_{ij}^{xy}S_i^x, \tag{5}$$

$$\frac{d}{dt}S_j^y = h_0 S_j^x + S\sum_i \left(J_{ij} - gD_{ij}^{xx}\right)S_i^x - gS\sum_i D_{ij}^{xy}S_i^y, \tag{6}$$

where $h_0$ is the static effective field along the $z$ axis,

$$h_0 = h + S\sum_i J_{ij} - gS\sum_i D_{ij}^{zz}. \tag{7}$$

We define the Fourier components

$$S_j^+ \equiv S_j^x + iS_j^y = \frac{1}{\sqrt{N}}\sum_{\vec{q}} S_l^+(\vec{q})e^{i\vec{q}\cdot\vec{r}_j}, \tag{8}$$

$$S_j^- \equiv S_j^x - iS_j^y = \frac{1}{\sqrt{N}}\sum_{\vec{q}} S_l^-(\vec{q})e^{-i\vec{q}\cdot\vec{r}_j}, \tag{9}$$

together with

$$J_{ij} \equiv \frac{1}{N}\sum_{\vec{q}} J_{ll'}(\vec{q})e^{i\vec{q}\cdot\vec{r}_{ij}}, \tag{10}$$

$$D_{ij}^{\alpha\beta} \equiv \frac{1}{N}\sum_{\vec{q}} D_{ll'}^{\alpha\beta}(\vec{q})e^{i\vec{q}\cdot\vec{r}_{ij}}, \tag{11}$$

where $l = 1,\ldots,L$ denotes the layer on which the spin $\vec{S}_j$ resides and $\vec{q} = (q_x, q_z)$ is the two-dimensional wave vector in the plane of the film. The linearized equations of motion may be written in matrix form as

$$-\mathbf{g}i\partial_t \begin{pmatrix} \mathbf{S}^+(\vec{q},t) \\ \mathbf{S}^-(-\vec{q},t) \end{pmatrix} = \begin{pmatrix} \mathbf{A}(\vec{q}) & \mathbf{B}(\vec{q}) \\ \mathbf{B}^\dagger(\vec{q}) & \mathbf{A}(\vec{q}) \end{pmatrix} \begin{pmatrix} \mathbf{S}^+(\vec{q},t) \\ \mathbf{S}^-(-\vec{q},t) \end{pmatrix}, \tag{12}$$

where $\mathbf{A}(\vec{q})$ and $\mathbf{B}(\vec{q})$ are $L \times L$ matrices with elements $A_{ll'}(\vec{q})$ and $B_{ll'}(\vec{q})$ given by

$$A_{ll'} = h_0\delta_{ll'} - S\left(J_{ll'}(\vec{q}) + \frac{g}{2}D_{ll'}^{zz}(\vec{q})\right), \tag{13}$$

$$B_{ll'} = \frac{gS}{2}\left[D_{ll'}^{xx}(\vec{q}) - D_{ll'}^{yy}(\vec{q}) + 2iD_{ll'}^{xy}(\vec{q})\right]. \tag{14}$$

$\mathbf{S}^+(\vec{q},t)$ and $\mathbf{S}^-(\vec{q},t)$ are $L$-component column matrices with components given by $S_l^+(\vec{q},t)$ and $S_l^-(\vec{q},t)$, respectively, and $\mathbf{g}$ is defined as the $2L \times 2L$ matrix,

$$\mathbf{g} = \begin{pmatrix} \mathbf{I} & \mathbf{0} \\ \mathbf{0} & -\mathbf{I} \end{pmatrix}. \tag{15}$$

The spin-wave modes correspond to solutions of the form

$$\begin{pmatrix} \mathbf{S}^+(\vec{q},t) \\ \mathbf{S}^-(-\vec{q},t) \end{pmatrix} = \mathbf{w}(\vec{q})e^{i\Omega t}. \tag{16}$$

It can be readily shown that, for each $\vec{q}$ vector, there are $2L$ such linearly independent solutions that satisfy the eigenvalue equation

$$\mathbf{g}\begin{pmatrix} \mathbf{A}(\vec{q}) & \mathbf{B}(\vec{q}) \\ \mathbf{B}^\dagger(\vec{q}) & \mathbf{A}(\vec{q}) \end{pmatrix}\mathbf{w}_\nu^\pm(\vec{q}) = \pm\Omega_\nu(\vec{q})\mathbf{w}_\nu^\pm(\vec{q}) \tag{17}$$

with $\nu = 1,\ldots,L$. Defining the $2L \times 2L$ matrix $\mathbf{W}$ as

$$\mathbf{W}(\vec{q}) = (\mathbf{w}_1^+(\vec{q})\cdots\mathbf{w}_L^+(\vec{q}), \mathbf{w}_1^-(\vec{q})\cdots\mathbf{w}_L^-(\vec{q})), \tag{18}$$

it can be shown that the eigenvectors may be normalized such that

$$\mathbf{W}^\dagger(\vec{q})\mathbf{g}\mathbf{W}(\vec{q}) = \mathbf{g} \tag{19}$$

and that the general solution to equation (12) may be written as

$$\begin{pmatrix} \mathbf{S}^+(\vec{q},t) \\ \mathbf{S}^-(-\vec{q},t) \end{pmatrix} = \sqrt{2}\mathbf{W}(\vec{q})\begin{pmatrix} \mathbf{c}(\vec{q})e^{i\Omega(\vec{q})t} \\ \mathbf{c}^*(-\vec{q})e^{-i\Omega(\vec{q})t} \end{pmatrix}, \tag{20}$$

where $\Omega_{\mu\nu}(\vec{q}) \equiv \delta_{\mu\nu}\Omega_\nu$ and $\mathbf{c}(\vec{q})$ and $\mathbf{c}^*(\vec{q})$ are two $L$-column vectors that define the spin-wave amplitudes and which are determined from the initial spin configuration as

$$\begin{pmatrix} \mathbf{c}(\vec{q}) \\ \mathbf{c}^*(-\vec{q}) \end{pmatrix} = \frac{1}{\sqrt{2}}\mathbf{g}\mathbf{W}^\dagger(\vec{q})\mathbf{g}\begin{pmatrix} \mathbf{S}^+(\vec{q},t=0) \\ \mathbf{S}^-(-\vec{q},t=0) \end{pmatrix}. \tag{21}$$

The spin-wave amplitudes $c_\nu(\vec{q})$ and $c_\nu^*(\vec{q})$ are the classical counterparts of magnon annihilation and creation operators in quantum-mechanical spin-wave theory. The transverse components of spin vectors, in the linear regime, may be expressed as a linear combination of the spin wave modes as

$$S_l^x(\vec{q},t) = \sum_{\nu=1}^{L}\left[\Phi_{l,\nu}e^{i\Omega_\nu t}c_\nu^*(\vec{q}) + \Phi_{l,\nu}^*e^{-i\Omega_\nu t}c_\nu(-\vec{q})\right], \tag{22}$$

$$S_l^y(\vec{q},t) = \sum_{\nu=1}^{L}\left[\Psi_{l,\nu}e^{i\Omega_\nu t}c_\nu^*(\vec{q}) + \Psi_{l,\nu}^*e^{-i\Omega_\nu t}c_\nu(-\vec{q})\right], \tag{23}$$

where

$$\Phi_{l\nu} = \frac{1}{\sqrt{2}}(w_{l\nu}^+ + w_{l\nu}^-), \tag{24}$$

$$\Psi_{l\nu} = \frac{1}{\sqrt{2}}(w_{l\nu}^+ - w_{l\nu}^-). \tag{25}$$

Expanding the energy given by Eq. (1) in powers of $\mathbf{c}(\vec{q})$ and $\mathbf{c}^*(\vec{q})$, we obtain

$$\mathcal{E} = \mathcal{E}_0 + \frac{1}{2}\sum_{\vec{q}}\begin{pmatrix} \mathbf{c}(\vec{q}) \\ \mathbf{c}^*(-\vec{q}) \end{pmatrix}^\dagger \begin{pmatrix} \Omega(\vec{q}) & \mathbf{0} \\ \mathbf{0} & \Omega(-\vec{q}) \end{pmatrix} \times \begin{pmatrix} \mathbf{c}(\vec{q}) \\ \mathbf{c}^*(-\vec{q}) \end{pmatrix} + \cdots \tag{26}$$

$$= \mathcal{E}_0 + \sum_{\vec{q}}\sum_\nu \Omega_\nu(\vec{q})c_\nu^*(\vec{q})c_\nu(\vec{q}) + \cdots, \tag{27}$$

where $\mathcal{E}_0$ denotes the ground-state energy of the system and the ellipses denote the higher-order terms in $\mathbf{c}(\vec{q})$ and $\mathbf{c}^*(\vec{q})$.

Accurately calculating the matrix elements for $\mathbf{A}(\vec{q})$ and $\mathbf{B}(\vec{q})$ requires considerable care due to the slow convergence of the dipolar sums in the terms $D_{ij}^{\alpha\beta}$. Calculations are performed using the methods described in Refs. 36 and 37. Results obtained from linearized spin-wave theory for several systems are presented in the next section.

### B. Numerical integration of the equations of motion

In addition to solving the eigenvalue equation, (17), from linearized spin-wave theory, the spectra for small amplitude spin waves can also be calculated from a spectral analysis

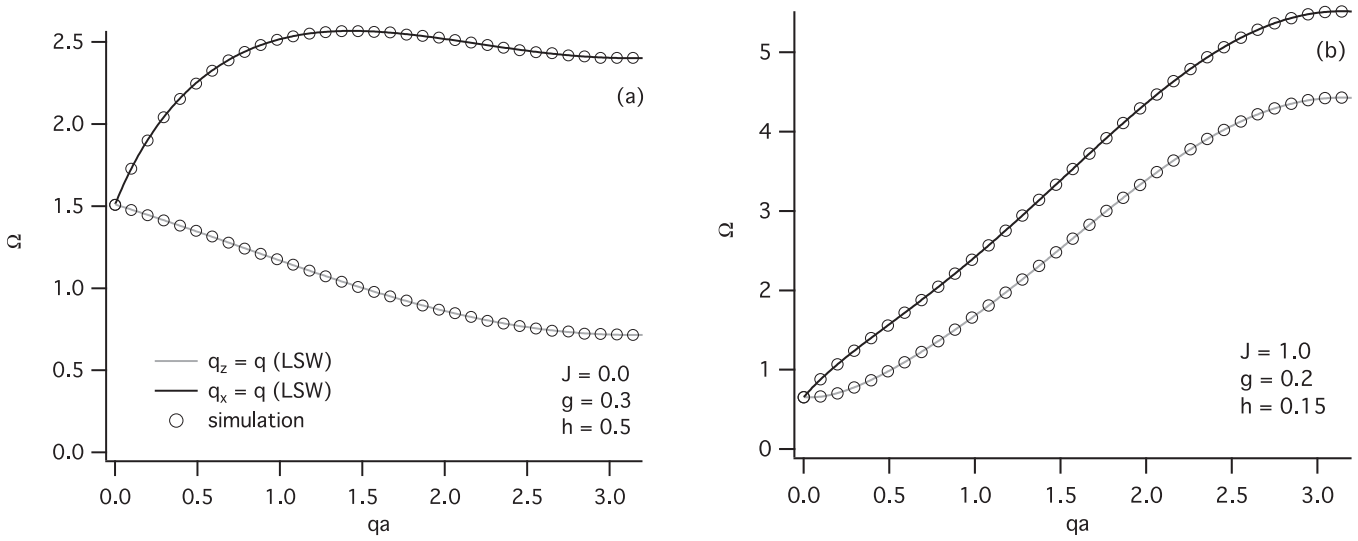


FIG. 1. Spin-wave frequency spectrum plotted as a function of the reduced wave number $qa$ for a ferromagnetic film composed of $N = 1$ layer for the (a) the pure dipolar case with $J = 0.0$, $g = 0.3$, and $h = 0.5$ and for (b) a dipole-exchange system with $J = 1.0$, $g = 0.2$, and $h = 0.15$ for $q_x = q$ and $q_z = q$. Solid lines are the results from linearized spin-wave theory and the circles are from the numerical integration of the equations of motion. In both cases, the black line (top) denotes the DE modes $[\vec{q} = (q,0)]$ while the gray line (bottom) denotes the BV modes $[\vec{q} = (0,q)]$.

of $S_l^{\alpha}(\vec{q},t)$ obtained by numerically integrating the equations of motion given by Eqs. (3) and (4). For this we consider a stacked lattice consisting of spins located on the vertices of $L$ layers of a $d \times d$ square lattice, with $S = 1$ and $J_{ij} = J > 0$ for nearest-neighbor spins and zero otherwise. We assume periodic boundary conditions in the $x$ and $z$ directions. Again, because of the slow convergence of the dipolar sums, care has to be taken in accurately calculating the dipolar contribution to the effective field. Also, in the absence of explicit damping, it is important that the integration procedure satisfies the constraint $|\vec{S}_i(t)| = S$. In the present work, the equation of motion for the spins is expressed in terms of quaternions and solved using a fourth-order Runge-Kutta algorithm. Details of the integration method are provided in Appendix A.

The spin-wave frequencies were calculated by generating a random initial state in which the polar angle of the spins is normally distributed about the $z$ axis with variance $\sigma$ and the azimuthal angle is uniformly distributed over the range $0 < \phi < \pi$. Since we wish to consider small-amplitude oscillations, the variance of the normal distribution satisfies the constraint $\sigma^2 \ll 1$ in order that nonlinear effects are negligible. $S^x(\vec{q},t)$ and $S^y(\vec{q},t)$ are then calculated over some finite-time domain $0 \leqslant t \leqslant t_{\max}$ by directly integrating the equations of motion using this perturbed state as the initial spin configuration. The spin-wave frequencies are then evaluated by determining the peaks in the power spectrum of $S^x(\vec{q},\omega)$ and $S^y(\vec{q},\omega)$. Each of the runs was performed using an initial spin configuration with $\sigma^2 = 5.77 \times 10^{-5}$ and an integration time step and run time given by $\Delta t = 5.0 \times 10^{-4}$ with $t_{\max} = 505.0$, respectively. Data were recorded to disk every 20 time steps ($20 \times \Delta t = 1.0 \times 10^{-2}$). In addition to the results presented here, numerous other runs were performed and it was determined that, provided the constraint on the variance $\sigma^2 \ll 1$ was satisfied, the resultant spin-wave spectra did not appear to depend on the initial conditions.

Dispersion curves for the single-layer case calculated from Eq. (17) and from the numerical integration of the equations of motion are presented in Fig. 1 for two sets of parameters. In Fig. 1(a), data are presented for the pure dipolar case with $J = 0.0$, $g = 0.3$, and $h = 0.5$. The dispersion curves for $\vec{q} = (q,0)$ and $\vec{q} = (0,q)$ illustrate the magnetostatic DE[9] modes and the backward volume (BV) modes, respectively, for the single-layer case. The DE mode is characterized by a rapid increase in frequency at long wavelength that saturates at short wavelengths. The BV mode, on the other hand, shows a monotonic decrease with increasing wave number with a well-defined minima at the zone boundary, $q_z = \pi/a$ reflecting the antiferromagnetic nature of the dipolar interaction.

Dispersion curves are presented for a dipole-exchange system with $J = 1.0$, $g = 0.2$, and $h = 0.15$ in Fig. 1(b). Comparing the dispersion curves in Fig. 1(a) with those in Fig. 1(b), we see that in the long-wavelength limit, the spin-wave frequencies are dominated by the long-range dipolar interaction and are independent of the exchange interaction for $q = 0$. As $q$ increases, the ferromagnetic nature of the exchange interaction starts to play a more important role, and the DE mode no longer saturates but increases with increasing $q$, while the minima in the BV mode has shifted away from zone boundary toward the zone center at $qa \approx 0.196$. Of particular interest for the present work is the good agreement between the spin-wave frequencies obtained from the eigenvalue equation and that obtained from the numerical integration of the equations of motion.

Results for the five-layer case are presented in Fig. 2 for two sets of parameters. Dispersion curves for the dipole case, with $J = 0.0$, $g = 0.3$, and $h = 0.5$, are presented in Figs. 2(a), $\vec{q} = (q,0)$, and 2(b), $\vec{q} = (0,q)$, with spin-wave frequencies calculated from both the eigenvalue equation (17) and the numerical integration of the equations of motion. The dispersion curves clearly show the very prominent DE surface

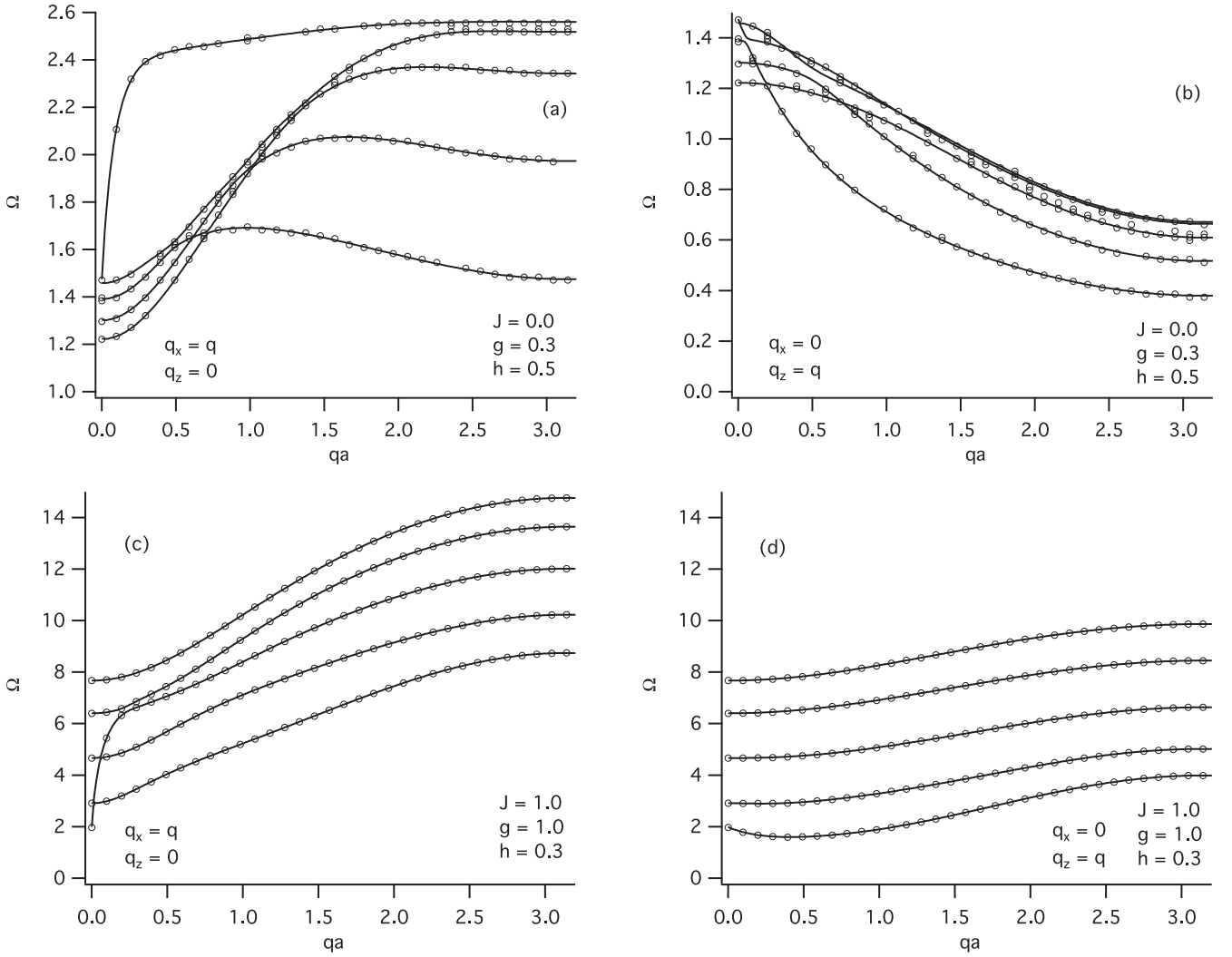


FIG. 2. Spin-wave frequency spectrum for a thin film composed of $N = 5$ layers plotted as a function of the reduced wave number $qa$ for the dipole system with parameters $J = 0.0$, $g = 0.3$, and $h = 0.5$ for (a) $\vec{q} = (q,0)$ and (b) $\vec{q} = (0,q)$ and the dipole-exchange system with $J = 1.0$, $g = 1.0$, and $h = 0.3$ for (c) $\vec{q} = (q,0)$ and (d) $\vec{q} = (0,q)$. Solid lines are the results from linearized spin-wave theory, and the circles are from the numerical integration of the equations of motion.

mode together with the four bulk modes, each corresponding to a distinct standing-wave pattern in the $z$ direction. The DE surface mode has the highest frequency at $q = 0$ and rises rapidly with increasing wave number. The data also show a considerable degree of mixing between the bulk modes. The corresponding data for $q_z = q$, presented in Fig. 2(b), show that the spin-wave frequencies decrease with increasing wave number, similar to the single-layer BV mode, with each having a minima at $q = \pi/a$. As with the BV mode in the single-layer case, this reflects the antiferromagnetic character of the dipolar interaction. The dispersion curves presented in Figs. 2(a) and 2(b) for the dipolar coupled system show a considerable degree of mixing with nearly degenerate frequencies over significant portions of the different branches. This quasidegeneracy of the spin-wave modes makes it difficult to extract distinct frequencies from the time series generated from numerical integration of the torque equation.

The effects of the exchange interaction on the dispersion curves can be seen in Figs. 2(c) and 2(d), where the frequencies for each of the five spin-wave modes calculated from the eigenvalue equation (17), and from the numerical integration of the equations of motion, are presented for a dipole-exchange system with $J = 1.0$, $g = 1.0$, and $h = 0.3$. Like the dipole case, the data in Fig. 2(a) show a very prominent DE surface mode together with four bulk modes, each corresponding to a distinct standing-wave pattern in the $z$ direction. However, a comparison between the dispersion curves shown in Figs. 2(a) and 2(c) demonstrates that the exchange interaction significantly modifies the $q = 0$ frequencies, with the DE surface mode frequency now below that of the four bulk modes. As the wave number increases, the DE surface mode frequency increases rapidly and mixes strongly with the bulk modes, to the extent that the DE mode and the four bulk spin-wave modes combine to form a band of exchange-dominated modes at larger $q$ values, as discussed in the Introduction.

The corresponding data for $q_z = q$, presented in Fig. 2(d), show that the ferromagnetic exchange compensates the antiferromagnetic dipolar interaction raising the frequencies from the values shown in Fig. 2(b) for the dipole case, such that all but the lowest mode increases with increasing $q$. For this

particular choice of parameters, the dipolar and exchange interactions combine to produce dispersion curves that are relatively flat. Again an important aspect of this comparison is the good agreement between the results of the linear spin-wave theory and those obtained from the numerical integration of the equations of motion.

Like the spin-wave spectra, the eigenvectors $\mathbf{w}_\nu^{\pm}$ defined by Eq. (17) are also strongly modified by the dipolar interaction, particularly at long wavelength, and can reveal important information about the structure of the spin waves in the case of multilayer lattices. To determine the spin-wave eigenfunctions from the numerical integration of the equations of motion, we define the dynamic correlation functions $C_l^{xx}(\vec{q},t)$ and $C_l^{yy}(\vec{q},t)$, which may be expressed in terms of the spin-wave eigenvectors, frequencies, and amplitudes as

$$C_l^{xx}(\vec{q},t) \equiv \lim_{T\to\infty}\frac{1}{T}\int_0^T S_l^x(\vec{q},t')S_l^x(\vec{q},t'+t)dt' = 2\sum_{\nu=1}^{L}|\Phi_{l,\nu}|^2|c_\nu(\vec{q})|^2\cos(\Omega_\nu(\vec{q})t), \tag{28}$$

$$C_l^{yy}(\vec{q},t) \equiv \lim_{T\to\infty}\frac{1}{T}\int_0^T S_l^y(\vec{q},t')S_l^y(\vec{q},t'+t)dt' = 2\sum_{\nu=1}^{L}|\Psi_{l,\nu}|^2|c_\nu(\vec{q})|^2\cos(\Omega_\nu(\vec{q})t) \tag{29}$$

together with the corresponding Fourier transforms

$$C_l^{xx}(\vec{q},\omega) \equiv \frac{1}{2\pi}\int_0^\infty C_l^{xx}(\vec{q},t)e^{i\omega t}dt = \lim_{\delta\to 0^+}\sum_{\nu=1}^{L}|\Phi_{l,\nu}|^2|c_\nu(\vec{q})|^2 \times\left(\frac{1}{\omega-\Omega_\nu(\vec{q})+i\delta}+\frac{1}{\omega+\Omega_\nu(\vec{q})+i\delta}\right), \tag{30}$$

$$C_l^{yy}(\vec{q},\omega) \equiv \frac{1}{2\pi}\int_0^\infty C_l^{xx}(\vec{q},t)e^{i\omega t}dt = \lim_{\delta\to 0^+}\sum_{\nu=1}^{L}|\Psi_{l,\nu}|^2|c_\nu(\vec{q})|^2 \times\left(\frac{1}{\omega-\Omega_\nu(\vec{q})+i\delta}+\frac{1}{\omega+\Omega_\nu(\vec{q})+i\delta}\right). \tag{31}$$

Thus we see that the quantities $|\Phi_{l,\nu}|^2|c_\nu(\vec{q})|^2$ and $|\Psi_{l,\nu}|^2|c_\nu(\vec{q})|^2$ may be readily obtained from $C_l^{xx}(\vec{q},\omega)$ and $C_l^{yy}(\vec{q},\omega)$, respectively.

To determine the amplitude of the spin-wave modes, we consider the dynamic correlation function $D(\vec{q},t)$ defined as

$$D(\vec{q},t) \equiv \lim_{T\to\infty}\frac{1}{T}\int_0^T\sum_l\left[S_l^y(\vec{q},t')S_l^x(\vec{q},t'+t) - S_l^x(\vec{q},t')S_l^y(\vec{q},t'+t)\right]dt' = 2\sum_\nu|c_\nu(\vec{q})|^2\sin[\Omega_\nu(\vec{q})t] \tag{32}$$

together with the corresponding Fourier transform

$$D(\vec{q},\omega) \equiv \frac{1}{2\pi}\int_0^\infty D(\vec{q},t)e^{i\omega t}dt = \lim_{\delta\to 0^+}\sum_{\nu=1}^{L} \times\left(\frac{|c_\nu(\vec{q})|^2}{\omega-\Omega_\nu(\vec{q})+i\delta}-\frac{|c_\nu(\vec{q})|^2}{\omega+\Omega_\nu(\vec{q})+i\delta}\right). \tag{33}$$

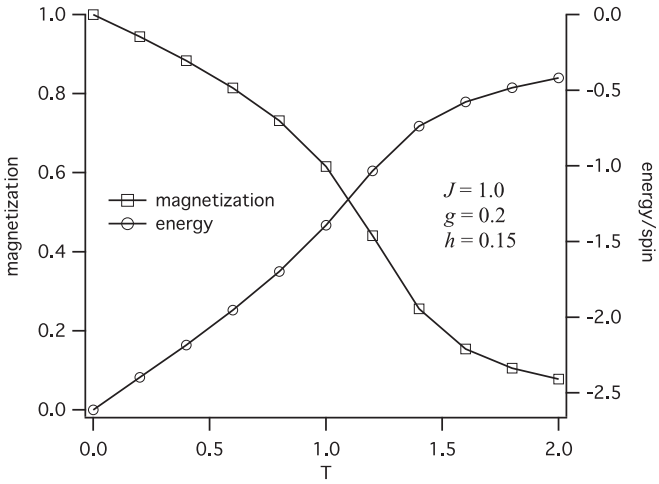


FIG. 3. Average energy and magnetization per spin calculated from Monte Carlo simulations for a $64 \times 64$ ferromagnetic lattice with $J = 1.0$, $g = 0.2$, and $h = 0.15$.

The correlation $D(\vec{q},\omega)$ is an extremely useful quantity as it provides a method to determine the spin-wave amplitudes $|c_\nu(\vec{q})|^2$ that does not rely on the specific nature of the eigenvectors $\Phi_{l,\nu}$ and $\Psi_{l,\nu}$. This property of the correlation function $D(\vec{q},\omega)$ is a direct consequence of the orthonormality of the eigenvectors expressed by Eq. (19).

## III. FINITE-TEMPERATURE SPIN WAVES

In this section, we apply the numerical integration methods described in the previous section to examine finite-temperature spin waves in a single ferromagnetic layer using Monte Carlo spin dynamics. We choose a system with $J = 1.0$, $g = 0.2$, and $h = 0.15$. The calculations are carried out on a square $64 \times 64$ lattice with $S = 1$. The magnetization and the energy of the system, calculated as a function of temperature from Monte Carlo simulations, are shown in Fig. 3. In each simulation, the system was initialized in the ground state with the spins aligned along the direction of the applied field. The system was then equilibrated for $2 \times 10^3$ Monte Carlo steps (MCS) before any data were recorded. The simulations were then run for a further $200 \times 10^3$ MCS with the net magnetization and energy recorded every 100 MCS and spin configurations recorded every $10^3$ MCS.

To evaluate the spin-wave dispersion curve at a given temperature $T$, the time series $S^x(\vec{q},t)$ and $S^y(\vec{q},t)$ were calculated by numerically integrating the equation of motion, using as an initial state one of the spin configurations generated from the Monte Carlo simulation. The integrations were performed using a second-order Runge-Kutta algorithm with $\Delta t = 1.0 \times 10^{-3}$ and $S^x(\vec{q},t)$ and $S^y(\vec{q},t)$ were recorded every 100 time steps for $0 \geqslant t \geqslant 5000$ for both $\{q_x = q, q_y = 0\}$ and $\{q_x = 0, q_y = q\}$. Three sample time series are shown in Fig. 4. The data clearly show the variation in the amplitude due to the thermal fluctuations. Less obvious is the variation in the phase constant of the oscillations arising from the thermal fluctuations. The effect of the variation in the phase constant may be observed in the correlation function $D(\vec{q},t)$, defined by Eq. (32). The correlation function calculated for the three

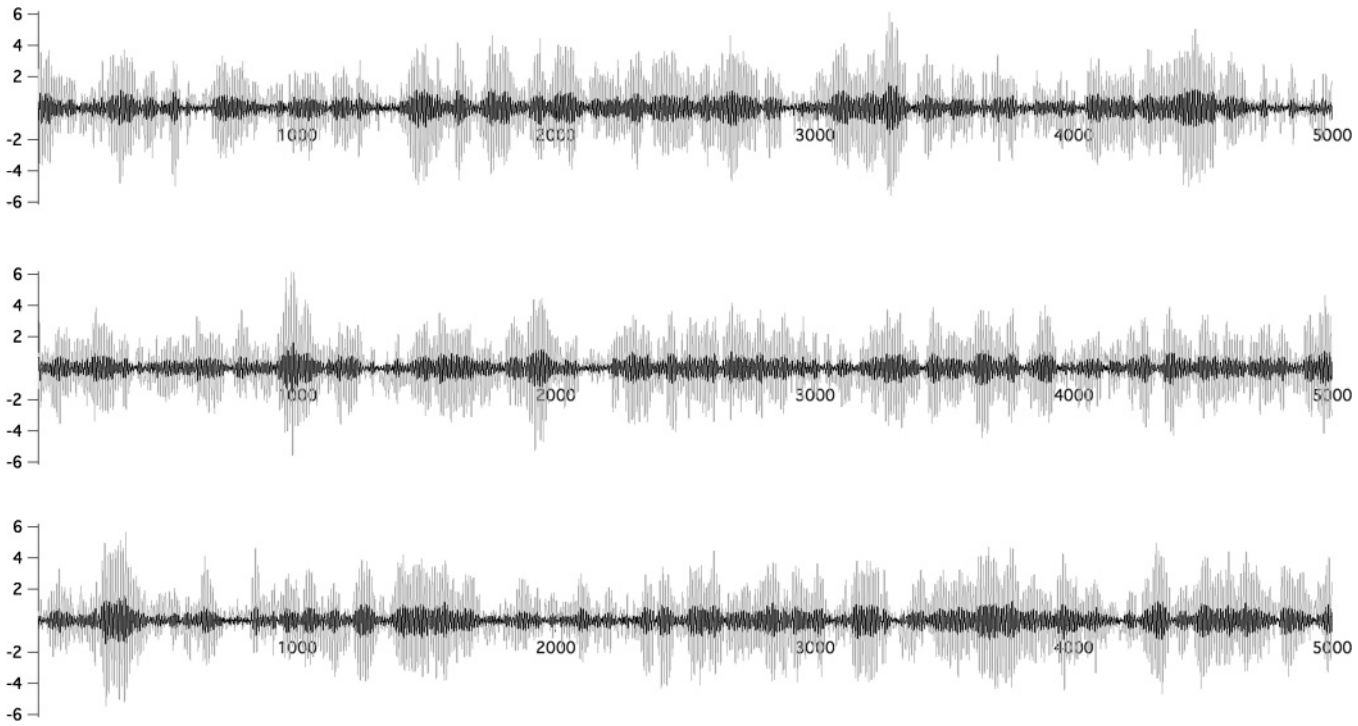


FIG. 4. Fourier-transformed fields $S^x(\vec{q},t)$ (black) and $S^y(\vec{q},t)$ (gray) plotted as a function of time over the range $0 \geqslant t \geqslant 5000$ for the particular case $q_x = q_z = 0$. Each time series is calculated from a different initial spin configuration generated by Monte Carlo simulation. Parameters are given by $T = 0.6$, $J = 1.0$, $g = 0.2$, and $h = 0.15$.

sample time series shown in Fig. 4 is presented in Fig. 5. The correlation function $D(\vec{q},t)$ was calculated by padding the finite time series $S_l^\alpha(\vec{q},t)$ by defining $S_l^\alpha(\vec{q},t+t_{\max}) \equiv S_l^\alpha(\vec{q},t)$, with $t_{\max} = 5000$. It can be readily shown that, because of the periodic nature of the padded time series, the correlation function is also periodic with $D(\vec{q},t) = D(\vec{q},t_{\max} - t)$. The data presented in Fig. 5 are plotted for the range $0 \leqslant t \leqslant 2500$. The variation in the amplitude of the correlation functions shown in Fig. 5 reflects the drift in the phase constant in the time-series data due to thermal fluctuations.

The spin-wave frequencies can be readily computed from the peaks in the power spectrum of the Fourier transform

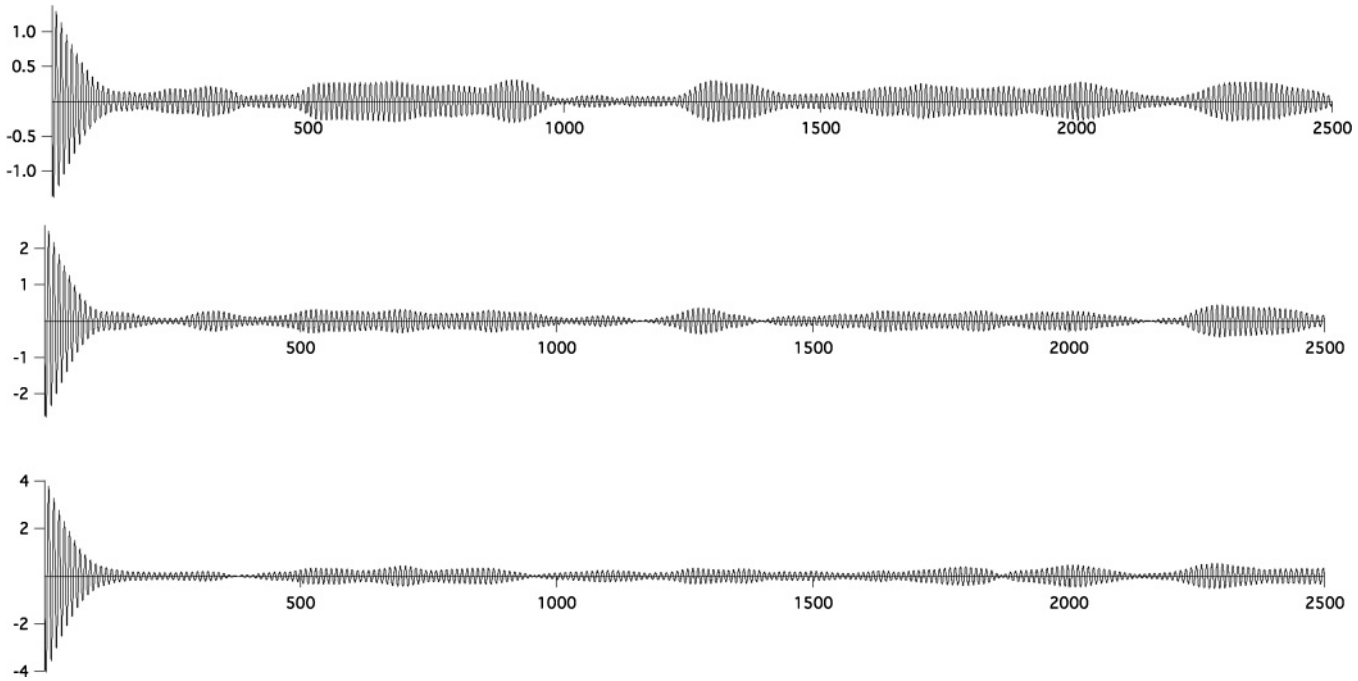


FIG. 5. Correlation function $D(\vec{q},t)$ defined by Eq. (32) plotted as a function of time over the range $0 \geqslant t \geqslant 2500$, calculated for each of the time series shown in Fig. 4. Parameters are given by $T = 0.6$, $J = 1.0$, $g = 0.2$, and $h = 0.15$.

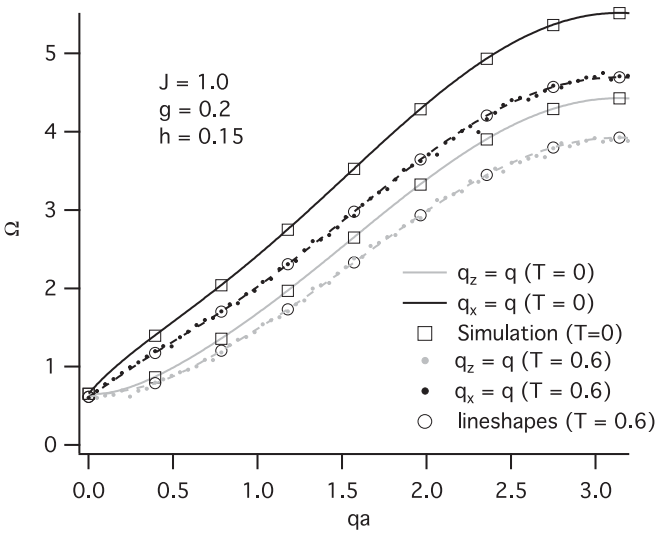


FIG. 6. Spin-wave frequencies plotted as a function of wave number for $J = 1$, $g = 0.2$, and $h = 0.15$ for $T = 0.0$ and 0.6. Solid lines represent the results from linear spin-wave theory with the black (top) lines and gray (bottom) lines corresponding to $\vec{q} = (q,0)$ and $(0,q)$, respectively. The open squares are the data obtained from the numerical integration of the equations of motion for $T = 0$, the dots are the results obtained from the numerical integration of the equations of motion for $T = 0.6$, and the open circles are the results obtained from the line-shape analysis of the finite-temperature correlation function $\langle D(\vec{q},\omega)\rangle$. The dashed lines are obtained by interpolating the finite $T$ results and are simply intended as a guide to the eye.

of the correlation function, $D(\vec{q},\omega)$. The dispersion curves calculated from a single time series are presented in Fig. 6, together with corresponding zero-temperature results. The finite-temperature spin-wave frequencies presented in Fig. 6 show a considerable degree of softening and scatter arising from the interaction between the large-amplitude fluctuations of the spin-wave modes.

The thermal average of the correlation function $\langle D(\vec{q},t)\rangle$ is given by

$$\langle D(\vec{q},t)\rangle \equiv \lim_{T\to\infty}\frac{1}{T}\int_0^T \sum_l \big[\langle S_l^y(\vec{q},t')S_l^x(\vec{q},t'-t)\rangle - \langle S_l^x(\vec{q},t')S_l^y(\vec{q},t'-t)\rangle\big]dt', \tag{34}$$

where the brackets $\langle\cdots\rangle$ denote the the propagator averaged over a canonical ensemble of initial states. Figure 7 shows the propagator for three values of $\vec{q}$ averaged over 200 distinct initial states generated from the Monte Carlo simulations, which clearly show the decay of the spin-wave oscillations. To understand the origin of this decay, it is important to keep in mind that our model does not include any explicit damping and that the numerical integration procedure is such that each of the 200 time series conserves energy to a high degree of numerical precision. This intrinsic damping of the spin waves arises as a consequence of the fact that the initial states used

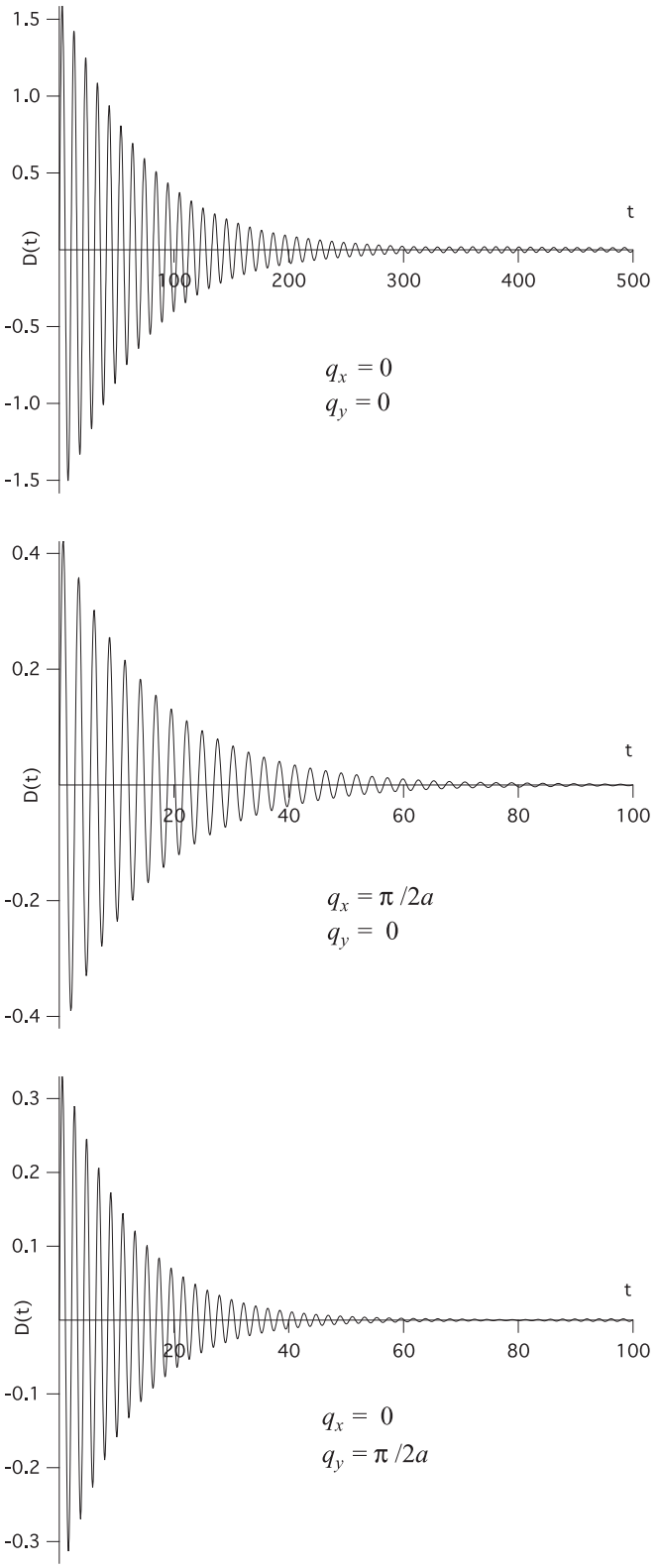


FIG. 7. Finite-temperature correlation function $\langle D(\vec{q},t)\rangle$, defined by Eq. (32), plotted as a function of time for (a) $\vec{q} = (0,0)$, (b) $\vec{q} = (\pi/2a,0)$, and (c) $\vec{q} = (0,\pi/2a)$. Parameters are given by $T = 0.6$, $J = 1.0$, $g = 0.2$, and $h = 0.15$.

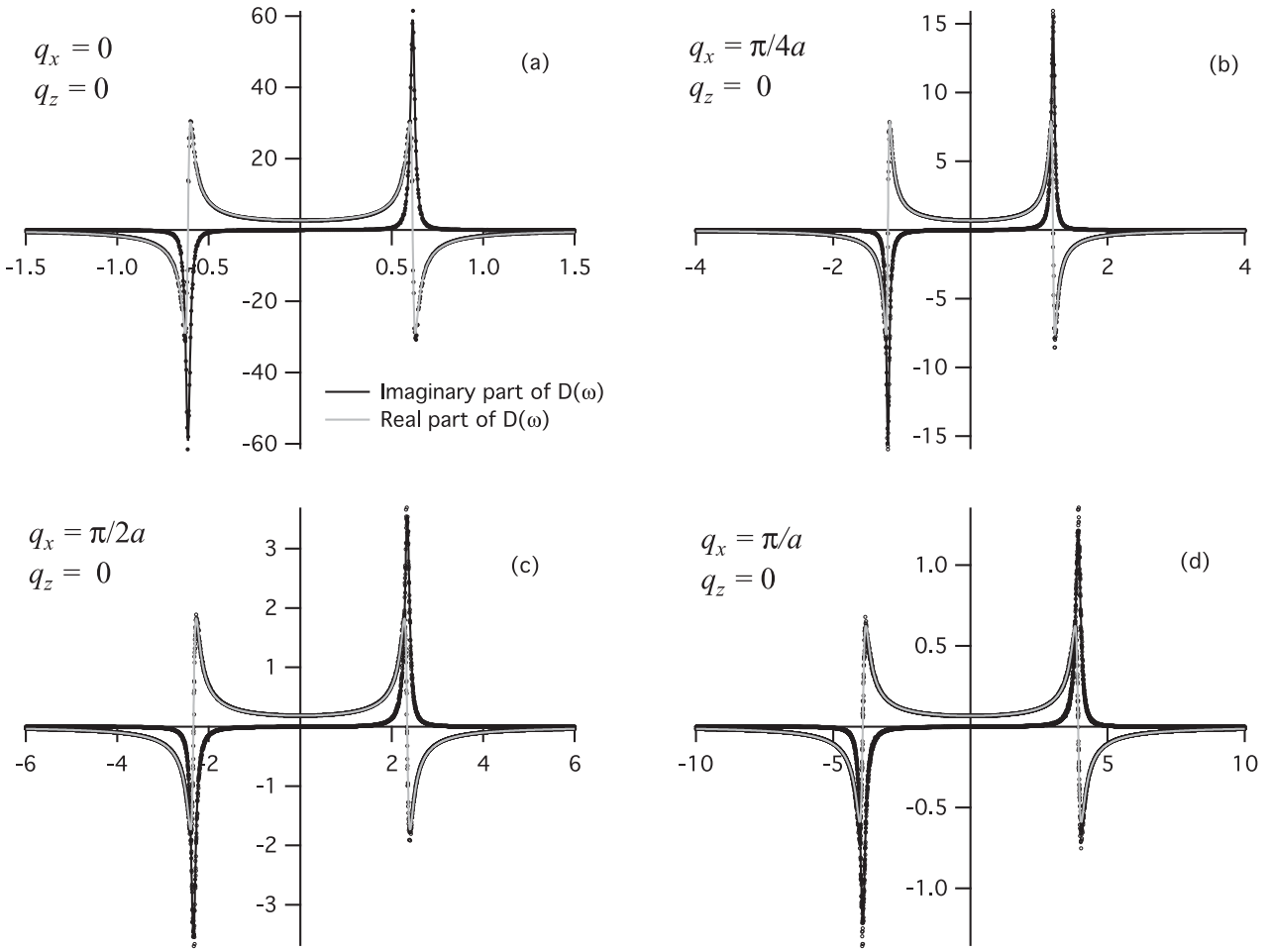


FIG. 8. Finite-temperature correlation function $D(\vec{q},\omega)$, defined by Eq. (33), plotted as a function of $\omega$ for (a) $\vec{q} = (0,0)$, (b) $\vec{q} = (\pi/4a,0)$, (c) $\vec{q} = (\pi/2a,0)$, and (c) $\vec{q} = (\pi/a,0)$. Points denote the data obtained from Monte Carlo spin dynamics and the lines show the fit to data using Eq. (36). The parameters are given by $T = 0.6$, $J = 1.0$, $g = 0.2$, and $h = 0.15$.

to calculate the time series are statistically independent and hence the drift in the phase constant due to thermal fluctuations will essentially randomize the phase of the correlations at long times. When we perform the ensemble average, this randomization of the phase will result in a considerable degree of cancellation at long times giving rise to the decrease in the amplitude of the oscillations observed in Fig. 7.

Assuming that the thermal average of the correlation function has the form given by Eq. (32), with $\Omega$ and $\delta$ replaced by the finite-temperature frequency and decay constant, we obtain

$$\langle D(\vec{q},t)\rangle = 2\langle|c_\nu(\vec{q})|^2\rangle \sin(\Omega(\vec{q})t)e^{-\Gamma(\vec{q})t}. \tag{35}$$

This yields a spectral function described by a double Lorentzian with poles located at $\omega = \pm\Omega(\vec{q}) - i\Gamma(\vec{q})$

$$\langle D(\vec{q},\omega)\rangle = \frac{\langle|c(\vec{q})|^2\rangle}{\omega + \Omega(\vec{q}) + i\Gamma(\vec{q})} - \frac{\langle|c(\vec{q})|^2\rangle}{\omega - \Omega(\vec{q}) + i\Gamma(\vec{q})}. \tag{36}$$

The Fourier transform $\langle D(\vec{q},\omega)\rangle$ for four separate values of $\vec{q}_x$ are presented in Fig. 8 for $T = 0.6$. Fitting the data to the spectral function given by Eq. (36) yields estimates for $\Omega(\vec{q})$, $\Gamma(\vec{q})$, and $\langle|c(\vec{q})|^2\rangle$. The fitted spectral functions are shown in Fig. 9 together with the simulation results. The good agreement between the fit and the simulation data indicates that, at $T = 0.6$, the form of the finite-temperature propagator given by Eq. (35) is a good approximation and hence the finite-temperature excitations may be described in terms of damped spin-wave modes with a temperature-dependent frequency and damping constant.

The finite-temperature correlation function $\langle D(\vec{q},\omega)\rangle$ has been calculated for several temperatures: $T = 0.2$, 0.4, 0.6, and 0.8, using the methods described above. The imaginary part of $\langle D(\vec{q},\omega)\rangle$ is plotted in Fig. 10 for several values of $\vec{q}$. The data show well-defined peaks that may be described in terms of damped spin-wave modes with a renormalized frequency $\Omega$ that decreases with increasing temperature and a decay constant $\Gamma$ that increases with increasing temperature. Fitting the simulation results to the spectral function defined by the imaginary part of Eq. (36) yields estimates of the renormalized frequency, decay constant, and amplitude. The

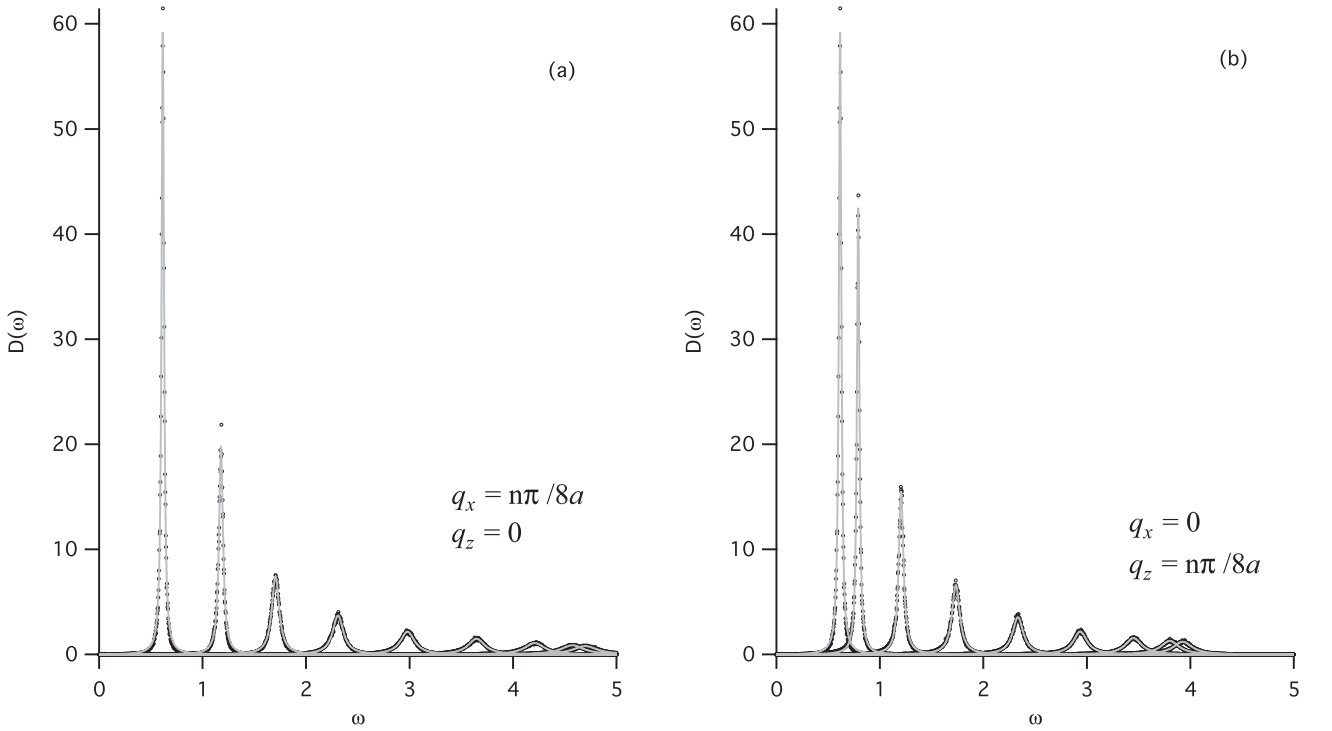


FIG. 9. The imaginary part of the finite-temperature correlation function $D(\vec{q},\omega)$, defined by Eq. (33), plotted as a function of $\omega$, for (a) $q_x = n\pi/8a$ with $q_z = 0$ and (b) $q_z = n\pi/8a$ with $q_x = 0$, with $T = 0.6$, $J = 1.0$, $g = 0.2$, $h = 0.15$, and $n = \{0,1,2,\ldots,8\}$. Points denote the data obtained from Monte Carlo spin dynamics and the lines show the fit to data using Eq. (36). The parameters are given by $T = 0.6$, $J = 1.0$, $g = 0.2$, and $h = 0.15$

resultant line shapes are plotted together with the simulation data in Fig. 10. The renormalized frequencies obtained from the fit are plotted in Fig. 11 for each of the above temperatures, together with the corresponding dispersion curves for $T = 0$. The dispersion curves illustrate how the spin-wave frequencies for $\vec{q} = (q,0)$ and $\vec{q} = (0,q)$ are renormalized by the thermal fluctuations.

In the case of a system of purely exchange coupled spins ($g = 0$) at $T = 0$ with Gilbert damping, the decay constant, for small-amplitude spin waves, is proportional to the frequency, with the proportionality constant equal to the dimensionless damping constant $\alpha$.[38] The damping constant $\alpha$ is an important parameter in the micromagnetic modeling of magnetic materials. In Fig. 12, the ratio $\Gamma/\Omega$ is plotted for $T = 0.2$, 0.4, 0.6, 0.8, and 1.0 over a range of $\vec{q}$ values. The data are plotted separately for the DE mode ($q_z = 0$) and the BV mode ($q_x = 0$). The data show the ratio $\Gamma/\Omega$ increases significantly with temperature and shows a marked dependence on frequency. It is also interesting, but not perhaps surprising, to note that the frequency dependence of the ratio is different for the DE mode and the BV mode.

In Fig. 13, $\langle|c(\vec{q})|^2\rangle/T$ is plotted as a function of $\Omega^{-1}(\vec{q})$. We see that the data are well described by a straight line passing close to the origin. This implies that, to a good approximation, the spin-wave energy is uniformly distributed across the spin-wave modes. For $T = 0.2$, a linear regression yields the relationship $|c|^2/T = m/\Omega + b$ with $m = 1.0147 \pm 0.0135$ and $b = -0.003\,881\,8 \pm 0.008\,18$, values that are consistent with the equipartition of energy $[\langle|c(\vec{q})|^2\rangle\Omega(\vec{q}) = T]$ to within one standard deviation. The values for the other temperatures are presented in Tabel I and show the slope decreasing and a small but systematic increase in the intercept with increasing temperature. The decrease in the slope $m$ from unity with increasing temperature suggests that the nonlinear terms in the spin-wave expansion of the energy, in addition to renormalizing the frequency of the spin-wave modes, also renormalize the spin-wave amplitudes.

From a computational perspective, it is important to note that the calculation of the decay constant $\Gamma(\vec{q})$ and the amplitude $\langle|c(\vec{q})|^2\rangle$ is considerably more computationally demanding that the calculation of the spin-wave frequencies due to the need to average over a sufficiently large ensemble, in this case 200 independent time series, to obtain accurate line shapes from the ensemble-averaged correlation function.

TABLE I. Spin-wave amplitude $|c(\vec{q})|^2/T = m/\Omega(\vec{q}) + b$.

| $T$ | 0.2 | 0.4 | 0.6 | 0.8 | 1.0 |
|---|---|---|---|---|---|
| $m$ | $1.015 \pm 0.013$ | $0.959 \pm 0.010$ | $0.849 \pm 0.010$ | $0.7574 \pm 0.0044$ | $0.6468 \pm 0.0086$ |
| $b$ | $-0.0039 \pm 0.0082$ | $-0.0091 \pm 0.0061$ | $0.0099 \pm 0.0069$ | $0.0202 \pm 0.0031$ | $0.0315 \pm 0.0069$ |

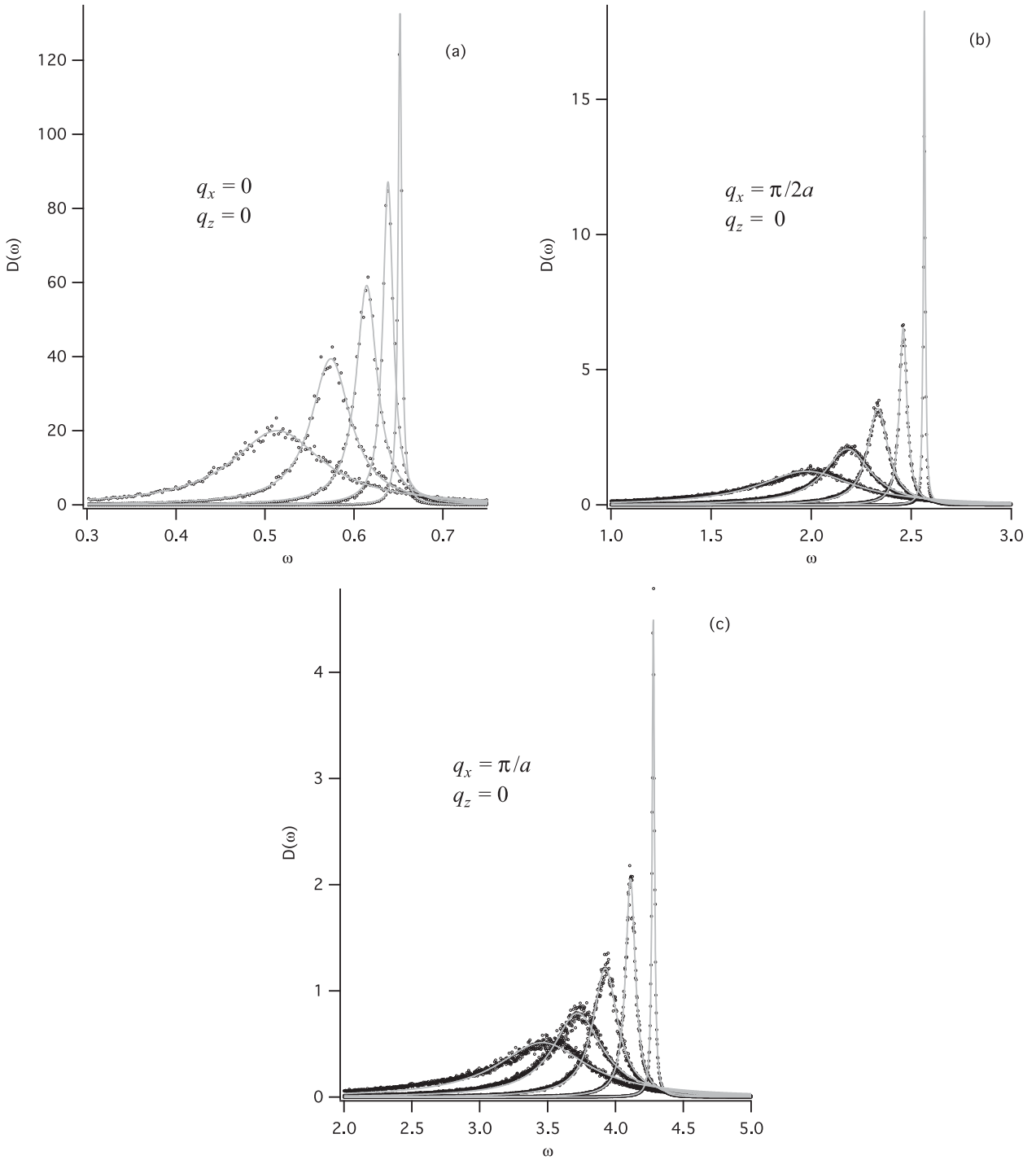


FIG. 10. The imaginary part of the correlation function $D(\vec{q},\omega)$, defined by Eq. (32), plotted as a function of $\omega$, for $T = 0.2$ (right), 0.4, 0.6, 0.8 and 1.0 (left) for (a) $q_x = 0$, (b) $\pi/2a$ and (c) $\pi/a$ with $q_z = 0$ with $J = 1.0$, $g = 0.2$ and $h = 0.15$. The data illustrate the softening of the frequency $\Omega$ and the increasing linewidth with increasing temperature and also show that, for $0.2 \leqslant T \leqslant 1.0$, the line shapes are well approximated by the double Lorentzian function given by Eq. (36).

## IV. DISCUSSIONS AND CONCLUSIONS

We have studied the properties of dipole-exchange spin waves in a planar ferromagnetic, both in the small-amplitude approximation and at finite temperature, where nonlinear effects are not negligible. Small-amplitude oscillation spin-wave dispersion curves were calculated for both single films and multilayers using both linearized spin-wave theory and by direct integration of the equations of motion. The results from both methods were compared and shown to be in very good agreement. The principal purpose of these calculations is to demonstrate how the properties of dipole-exchange spin waves in thin films could be calculated by direct numerical integration of the equation of motion and that the results are consistent with those obtained from linearized spin-wave theory. Both

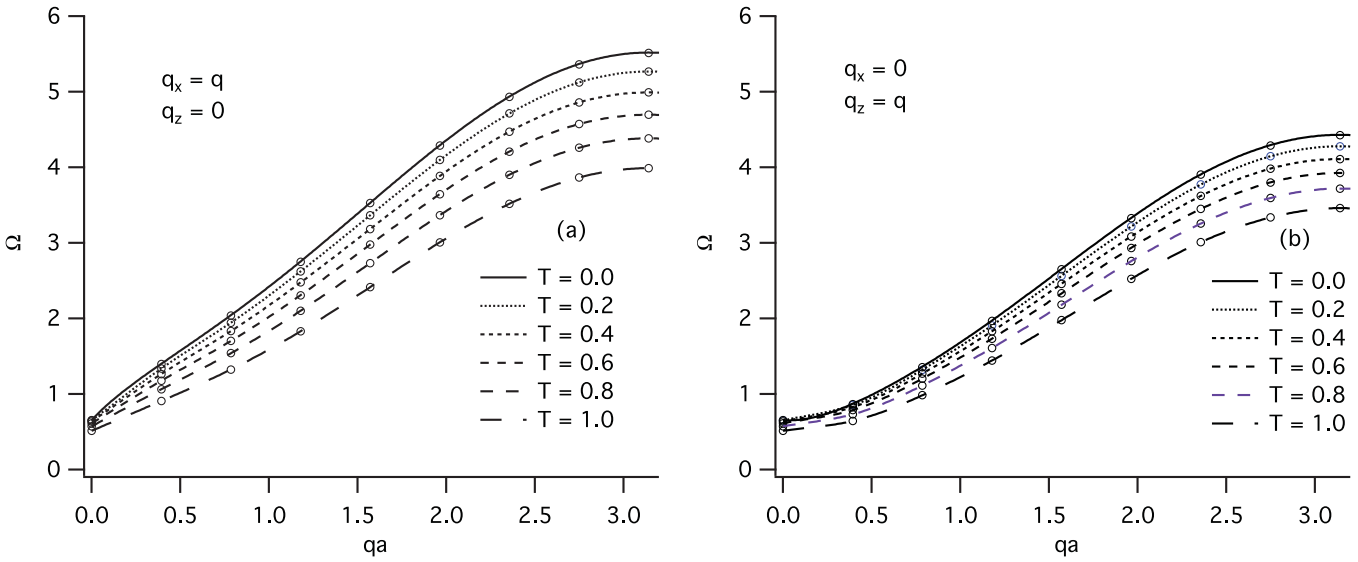


FIG. 11. Dispersion curves for $T = 0.2, 0.4, 0.6, 0.8$, and 1.0. Circular markers are calculated from simulation data, while lines for $T = 0.2$, 0.4, 0.8, and 1.0 are obtained by interpolation and are intended as a guide to the eye.

methodologies can be extended to include more complex geometries, lattice structures (including antiferromagnetic structures), and interactions. From a computational perspective, the two methods are complementary in the limit of small-amplitude spin-wave excitations. While the formulation of the linearized spin-wave theory of dipole-exchange spin waves in complex geometries is mathematically more involved, it imposes a relatively modest computational burden. By contrast, the direct integration of the equations of motion, while computationally more demanding, can be readily applied to a wide range of complex geometries and interactions.

One obvious advantage of the numerical integration method over the linearized spin-wave theory is that it is not limited to small-amplitude oscillations and it is straightforward to apply the methodology developed for small-amplitude spin-wave modes to finite temperature using Monte Carlo spin dynamics. Monte Carlo spin dynamics takes an ensemble of statistically independent spin configurations generated from a Monte Carlo simulation and calculates the time evolution of each of these spin configurations by direct integration of the equation of motion. The finite-temperature correlation functions are then obtained by averaging the correlation function for each of the trajectories over the entire ensemble. As discussed in the Introduction, this method has been successfully applied to study finite-temperature spin dynamics in a variety two- and three-dimensional exchange coupled systems.

Monte Carlo spin dynamics was applied to a $64 \times 64$ square lattice with $J = 1.0$, $g = 0.2$, and $h = 0.15$ for several temperatures $T = 0.2, 0.4, 0.6, 0.8$, and 1.0. Examples of the time series for $S^x(\vec{q},t)$ and $S^y(\vec{q},t)$ for $T = 0.6$ are shown in Fig. 4 together with the corresponding correlation function $D(\vec{q},t)$ in Fig. 5. The dispersion curve calculated from the peaks in $D(\vec{q},t)$ is presented for $T = 0.6$ together with the corresponding dispersion curve for $T = 0.0$ in Fig. 6, and they clearly show the expected softening of the spin-wave frequencies. Accurately calculating the line shapes of the spin-wave modes is somewhat more difficult than simply extracting the frequencies, as this required averaging over a large number of extended runs. The finite-temperature correlation function $\langle D(\vec{q},t)\rangle$ and the corresponding Fourier transform $\langle D(\vec{q},\omega)\rangle$ for $T = 0.6$ are plotted in Figs. 7 and 8, respectively, for several values of $\vec{q}$. The data for $\langle D(\vec{q},t)\rangle$ that describe an exponentially decaying spin-wave mode with $\langle D(\vec{q},\omega)\rangle$ approximated a double Lorentzian line shape, corresponding to poles just below the real axis at $\omega = \pm\Omega(\vec{q}) - i\Gamma(\vec{q})$. As the calculations do not include any form of explicit damping, the decay of the spin-wave mode observed in $\langle D(\vec{q},t)\rangle$ may be entirely attributed to the effect of thermal fluctuations.

A similar analysis of the time series obtained for the other temperatures yields the dispersion curves shown in Fig. 11 and the line shapes obtained from the correlation function in Fig. 10. The data show how the frequency and decay constants change with temperature. Plots of the ratio $\Gamma(\vec{q})/\Omega(\vec{q})$ as a function of $q$ for both $\vec{q} = (q,0)$ and $\vec{q} = (0,q)$ are presented in Fig. 12 for each of the temperatures studied. The data show that the ratio is strongly temperature-dependent and demonstrates a relatively weak dependence on $q$ that is different for the transverse $\vec{q} = (q,0)$ and the longitudinal $\vec{q} = (0,q)$ modes. As pointed out in the text, this ratio is closely related to the Gilbert damping constant used in the Landau-Lifshitz-Gilbert (LLG) equation, however since the analysis does not include any explicit damping, this plot gives some indication of the significance of the intrinsic damping in dipole-exchange coupled films at finite temperature.

The final graph (Fig. 13) shows the spin-wave amplitude $|c(\vec{q})|^2/T$ plotted as a function of $1/\Omega(\vec{q})$ for each of the temperatures studied. The data suggest that while for the temperatures studied the thermal energy is distributed evenly across the various modes, the ratio $|c(\vec{q})|^2\Omega(\vec{q})/T < 1$ and decreases with increasing temperature, implying that the spin-wave amplitudes are renormalized by the thermal fluctuations.

The results presented in Sec. III indicate that, at least for some of the lower temperatures studied, the spin-wave modes are only weakly renormalized by the thermal fluctuations and therefore should be amenable to analysis in terms

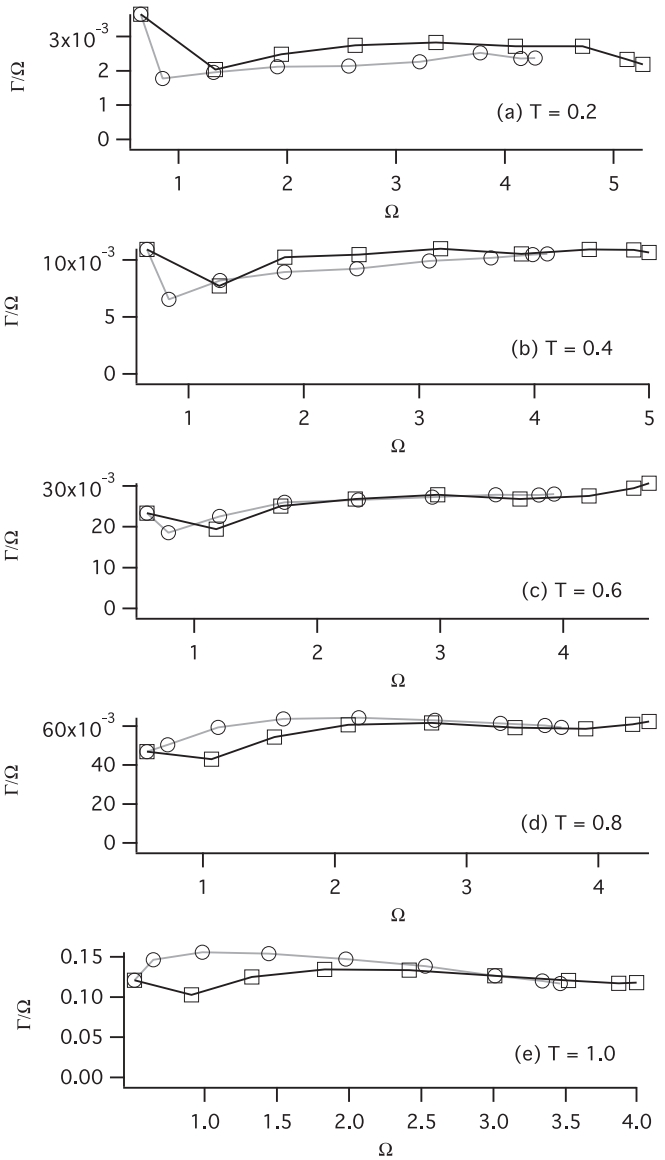


FIG. 12. The ratio $\Gamma/\Omega$ plotted as a function of $\Omega$ plotted for several temperatures. The points are obtained from the fit to the results obtained from Monte Carlo spin dynamics for both $\vec{q} = (q,0)$ (squares) and $\vec{q} = (0,q)$ (circles). The lines joining the markers are simply a guide to the eye.

of finite-temperature perturbation theory.[20] We have also extended these calculations to include temperatures beyond those presented in the present work. At higher temperatures, the data show a broadening of the line shapes associated with the spin-wave modes and the presence of a diffusive mode associated with the longitudinal fluctuations. We are currently analyzing these data and hope to obtain a systematic description the temperature dependence of the excitation spectra that can be compared with theoretical models.

In addition to spin-wave spectra, the ability to study the nonlinear effects of large-amplitude excitation can be applied to a number of other problems of interest related to the dynamics of magnetic thin films. Such examples include large-amplitude FMR studies[39] and the nonlinear amplification of spin waves,[40] which have been the subject

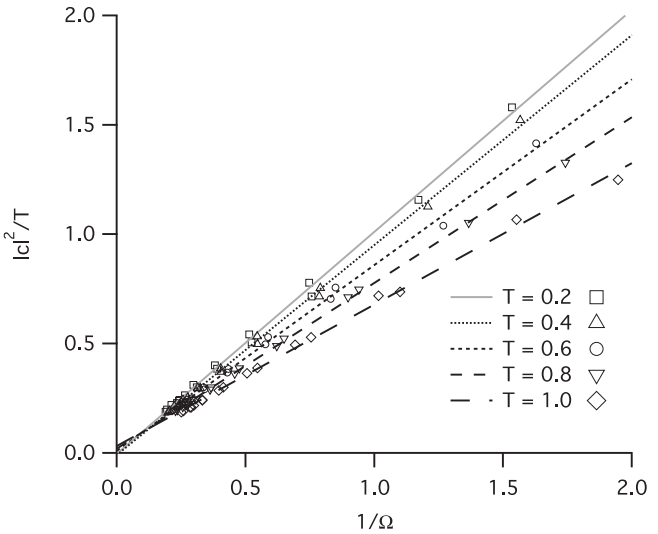


FIG. 13. The ratio $\langle |c(\vec{q})|^2 \rangle / T$ plotted as a function of $\Omega(\vec{q})^{-1}$ for several temperatures, together with the line of best fit for each passing through the origin. The slope of the line is equal to the energy per mode due the thermal fluctuations.

of recent experimental and theoretical interest. It would also be instructive to compare the results of the Monte Carlo spin dynamics with the corresponding results obtained using the stochastic LLG equation, which would presumably combine the effects of the intrinsic damping arising from the thermal fluctuations with the explicit Gilbert damping. Identifying and quantifying the contribution of intrinsic and explicit damping to the excitation spectra in dipole-exchange magnetic thin films would provide important insight into the parametrization and application of finite-temperature micromagnetics.

## ACKNOWLEDGMENTS

The authors would like to thank Dr. M. Cottam and Dr. A. B. Macisaac, University of Western Ontario, for helpful discussions in the course of this work, and K. Sooley for assistance with the simulations. One the authors (T.M.N.) gratefully acknowledges financial support from the ACEnet. Computational facilities were provided by ACEnet, the regional high performance computing consortium for universities in Atlantic Canada and the Centre for Magnetic Materials and Simulation at Memorial University. This work was supported by grants from Natural Sciences and Engineering Research Council of Canada.

## APPENDIX A: NUMERICAL INTEGRATION OF THE EQUATIONS OF MOTION

The torque equation given by Eq. (3) describes the precession of the spin vector $\vec{S}_i$ about the effective field $\vec{h}_i$ with an angular frequency $\omega_i = h_i$. The solution of this system of equations consists of two parts: (i) calculating the effective fields $\{\vec{h}_i\}$ for a given spin configuration $\{\vec{S}_i\}$, from which (ii) we determine both the axis and angular frequency of the resultant precession. These two tasks are coupled as both the effective fields and the spin configuration must be determined self-consistently. The evaluation of the effective field is

complicated by the long-range character of the dipolar interaction, and although it represents a significant computational task, it is nevertheless relatively straightforward.

In the simulations, we consider only spin configurations that are periodic in both the $x$ and the $z$ directions such that

$$\vec{S}(\vec{r} + mda\hat{i} + ndak\hat{)} = \vec{S}(\vec{r}) \tag{A1}$$

and they are therefore completely specified in terms of the set of $N_d = L \times d^2$ vectors $\{\vec{S}_i\}$. The periodicity requirement limits the range of $\vec{q}$ values for which we can calculate the spin-wave frequencies to the $d^2$ set of reciprocal-lattice vectors $\vec{q} = 2\pi n/d$. The dipolar contribution to the effective field may be evaluated as a sum over equivalent lattice sites:

$$\begin{aligned}\vec{h}_i^{\,\mathrm{dip}} \cdot \hat{e}^\alpha &= g \sum_j \left( \frac{\delta_{\alpha\beta}}{r_{ij}^3} - 3\frac{r_{ij}^\alpha r_{ij}^\beta}{r_{ij}^5} \right) S_j^\beta \\ &= g \sum_j^{N_d} \sum_{\vec{R}}^{N/N_d} \left( \frac{\delta_{\alpha\beta}}{|\vec{r}_{ij} - \vec{R}|^3} - 3\frac{(r_{ij}^\alpha - R^\alpha)(r_{ij}^\beta - R^\alpha)}{|\vec{r}_{ij} - \vec{R}|^5} \right) S_j^\beta \\ &= \sum_j^{N_d} d^{\alpha\beta}(\vec{r}_{ij}) S_j^\beta . \end{aligned} \tag{A2}$$

The effective interaction $d^{\alpha\beta}(\vec{r}_{ij})$ defined as

$$d^{\alpha\beta}(\vec{r}_{ij}) = \sum_{\vec{R}}^{N/N_d} \left( \frac{\delta_{\alpha\beta}}{|\vec{r}_{ij} - \vec{R}|^3} - 3\frac{(r_{ij}^\alpha - R^\alpha)(r_{ij}^\beta - R^\alpha)}{|\vec{r}_{ij} - \vec{R}|^5} \right) \tag{A3}$$

may be evaluated by a number of methods to improve convergence, such as the Ewald summation technique.[7]

The periodic nature of the spin configuration allows us to write the above expression in terms of the Fourier transforms of the effective dipolar field and the spin configuration as

$$h_n^\alpha(\vec{q}) = \sum_{\beta n'} d_{nn'}^{\alpha\beta}(\vec{q}) S_{n'}^\beta(\vec{q}). \tag{A4}$$

Given that the effective fields can be calculated for a given spin configuration, there are a number of methods that can be used to integrate the resultant torque equation. However, in selecting a particular integration scheme, it is important that it preserve both the magnitude of the spin variables $\{\vec{S}_i\}$ and the energy. One approach used to address this issue in exchange coupled systems is based on the Suzuki-Trotter decompositions of exponential operators.[41] Because of the long-range nature of the dipolar interaction, in the present work we instead calculate the precession about the effective field by means of a rotation using quaternions. The spin vectors at time $t + \Delta t$ may be written in terms of their orientation at time $t$ as

$$\vec{S}_i(t + \Delta t) = \vec{R}(\hat{h}_i, h_i \Delta t) \cdot \vec{S}_i(t), \tag{A5}$$

where $\vec{R}(\hat{e}, \Delta\theta)$ denotes the rotation matrix describing a rotation of angle $\Delta\theta$ about an axis directed along the unit vector $\hat{e}_i$ and $\hat{h}_i = \vec{h}_i / h_i$. Here we have assumed that $\Delta t$ is sufficiently small that the effective fields $\{\vec{h}_i\}$ may be assumed constant. This ensures that the magnitude of the spin vector is constrained such that $|\vec{S}_i(t)| = S$. It is computationally efficient to describe the rotation given by Eq. (A5) using quaternions as opposed to the three-dimensional rotation vector.[42]

A quaternion $\mathbb{V}$ and its conjugate $\mathbb{V}^*$ are defined as tuples constructed from a scalar quantity $u$ and a vector $\vec{v}$ as

$$\begin{aligned}\mathbb{V} &= \{u, \vec{v}\}, \\ \mathbb{V}^* &= \{u, -\vec{v}\}.\end{aligned}$$

Quaternion algebra defines the product of two quaternions as

$$\mathbb{V}_1 \mathbb{V}_2 = \{u_1 u_2 - \vec{v}_1 \vec{v}_2, u_1 \vec{v}_1 + u_2 \vec{v}_2 + \vec{v}_1 \times \vec{v}_1\}.$$

If we embed a vector $\vec{v}$ in a quaternion $\mathbb{V}$ as

$$\mathbb{V} = \{0, \vec{v}\}, \tag{A6}$$

then the vector $\vec{v}'$ defined by rotation of the vector $\vec{v}$ by an angle $\theta$ about an axis represented by the unit vector $\hat{e}$ may be expressed in terms of the product

$$\mathbb{V}' = \mathbb{Z}(\hat{e}, \theta) \mathbb{V} \mathbb{Z}^*(\hat{e}, \theta), \tag{A7}$$

where the quaternion quantity $\mathbb{Z}(\vec{\hat{e}}, \theta)$ is defined as

$$\mathbb{Z}(\hat{e}, \theta) = \{\cos(\theta/2), \sin(\theta/2)\hat{e}\} \tag{A8}$$

and the rotated vector $\vec{v}'$ is given by the vector part of the quaternion $\mathbb{V}' = \{u', \vec{v}'\}$. Since the scalar part of $\mathbb{V}'$ does not need to be calculated, the evaluation of $\vec{v}'$ from $\vec{v}$ requires two fewer floating point multiplications per rotation than using the explicit rotation matrix defined by Eq. (A5).

Equation (A5) may then be expressed in quaternion notation as

$$\mathbb{S}i^{t+\Delta t} = \mathbb{Z}_i^t \mathbb{S}_i^t \mathbb{Z}_i^{t*} \tag{A9}$$

with

$$\mathbb{S}_i^t = \{0, \vec{S}_i(t)\}, \tag{A10}$$

$$\mathbb{Z}_i^t = \left\{ \cos\left(\frac{h_i(t)}{2}\right), \hat{h}_i(t) \sin\left(\frac{h_i(t)}{2}\right) \right\}, \tag{A11}$$

$$\mathbb{S}_i^{t+\Delta t} = \{u, \vec{S}_i(t + \Delta t)\}, \tag{A12}$$

where $u$ is an uncomputed scalar.

Quaternions allow higher-order integration schemes to be implemented succinctly. Noting that $\mathbb{Z}_i$ may be computed from $\mathbb{S}_i$, the second-order Runge-Kutta scheme may be expressed as

$$\mathbb{S}_i^{t+\Delta t/2} = \tilde{\mathbb{Z}}_i^t \mathbb{S}_i^t \tilde{\mathbb{Z}}_i^{t*}, \tag{A13}$$

$$\mathbb{S}_i^{t+\Delta t} = \mathbb{Z}_i^{t+\Delta t/2} \mathbb{S}_i^t \mathbb{Z}_i^{t+\Delta t/2*}, \tag{A14}$$

where $\tilde{\mathbb{Z}}_i^t$ denotes the half-rotation form of $\mathbb{Z}_i^t$,

$$\tilde{\mathbb{Z}}_i^t = \left\{ \cos\left(\frac{h_i(t)}{4}\right), \hat{h}_i(t) \sin\left(\frac{h_i(t)}{4}\right) \right\}. \tag{A15}$$

Quaternion and rotation methods are, in general, better at conserving energy than methods that treat the Cartesian components separately.

*Author to whom all correspondence should be addressed: johnw@mun.ca


[1] J. Prokop, W. X. Tang, Y. Zhang, I. Tudosa, T. R. F. Peixoto, Kh. Zakeri, and J. Kirschner, Phys. Rev. Lett. **102**, 177206 (2009).

[2] Kh. Zakeri, Y. Zhang, J. Prokop, T.-H. Chuang, N. Sakr, W. X. Tang, and J. Kirschner, Phys. Rev. Lett. **104**, 137203 (2010).

[3] D.-S. Han, S.-K. Kim, J.-Y. Lee, S. J. Hermsdoerfer, H. Schultheiss, B. Leven, and B. Hillebrands, Appl. Phys. Lett. **94**, 112502 (2009).

[4] S. Schwieger, J. Kienert, K. Lenz, J. Lindner, K. Baberschke, and W. Nolting, Phys. Rev. Lett. **98**, 057205 (2007).

[5] *Ultrathin Magnetic Structures IV*, edited by B. Heinrich and J. C. Bland (Springer, Berlin, 2005).

[6] O. G. Heinonen, D. K. Schreiber, and A. K. Petford-Long, Phys. Rev. B **76**, 144407 (2007).

[7] K. De'Bell, A. B. MacIsaac, and J. P. Whitehead, Rev. Mod. Phys. **72**, 225 (2000).

[8] J. P. Whitehead, A. B. MacIsaac, and K. De'Bell, Phys. Rev. B **77**, 174415 (2008).

[9] R. W. Damon and J. R. Eshbach, J. Phys. Chem. Solids **19**, 308 (1961).

[10] H. Benson and D. L. Mills, Phys. Rev. **178**, 839 (1969).

[11] B. A. Kalinikos and A. N. Slavin, J. Phys. C **19**, 7013 (1986).

[12] R. P. Erickson and D. L. Mills, Phys. Rev. B **43**, 10715 (1991).

[13] M. G. Cottam, *Linear and Nonlinear Spin Waves in Magnetic Films and Superlattices* (World Scientific, Singapore, 1994); D. D. Stancil, *Theory of Magnetostatic Waves* (Springer-Verlag, New York, 1993).

[14] J. R. Dutcher, J. F. Cochran, I. Jacob, and W. F. Egelhoff, Phys. Rev. B **39**, 10430 (1989).

[15] H. T. Nguyen and M. G. Cottam, Surf. Rev. Lett. **15**, 727 (2008).

[16] H. T. Nguyen and M. G. Cottam, Surf. Rev. Lett. **15**, 727 (2008); **72**, 224415 (2005); J. Magn. Magn. Mater. **310**, 2433 (2007).

[17] H. T. Nguyen, T. M. Nguyen, and M. G. Cottam, Phys. Rev. B **76**, 134413 (2007).

[18] G. Gubbiotti, S. Tacchi, G. Carlotti, P. Vavassori, N. Singh, S. Goolaup, A. O. Adeyeye, A. Stashkevich, and M. Kostylev, Phys. Rev B **72**, 224413 (2005).

[19] T. M. Nguyen, M. G. Cottam, H. Y. Liu, Z. K. Wang, S. C. Ng, M. H. Kuok, D. J. Lockwood, K. Nielsch, and U. Gosele, Phys. Rev. B **73**, 140402 (2006).

[20] R. N. Costa Filho , M. G. Cottam, and G. A. Farias, Phys. Rev. B **62**, 6545 (2000).

[21] S. Henning, F. Kormann, J. Kienert, W. Nolting, and S. Schwieger, Phys. Rev. B **75**, 214401 (2007).

[22] C. Kawabata and A. Bishop, Solid State Commun. **42**,595 (1982).

[23] G. M. Wysin and A. R. Bishop, Phys. Rev. B **42**, 810 (1990).

[24] D. A. Dimitrov and G. M. Wysin, Phys. Rev. B **53**, 8539 (1996).

[25] M. E. Gouvêa, G. M. Wysin, S. A. Leonel, A. S. T. Pires, T. Kamppeter, and F. G. Mertens, Phys. Rev. B **59**, 6229 (1999).

[26] G. M. Wysin, M. E. Gouvêa, and A. S. T. Pires, Phys. Rev. B **62**, 11585 (2000).

[27] K. Chen and D. P. Landau, Phys. Rev. B **49**, 3266 (1994).

[28] M. Krech and D. P. Landau, Phys. Rev. B **60**, 3375 (1999).

[29] K. Nho and D. P. Landau, Phys. Rev. B **66**, 174403 (2002).

[30] X. Tao, D. P. Landau, T. C. Schulthess, and G. M. Stocks, Phys. Rev. Lett. **95**, 087207 (2005).

[31] D. P. Landau and M. Krech, J. Phys. Condens. Matter **11**, R179 (1999).

[32] *The Physics of Ultra-High-Density Magnetic Recording*, edited by M. Plumer, J. van Ek, and D. Weller (Springer-Verlag, Berlin, 2001).

[33] R. Chaudhury, J. Magn. Magn. Mater. **307**, 99 (2006).

[34] E. Meloche, C. M. Pinciuc, and M. L. Plumer, Phys. Rev. B **74**, 094424 (2006); E. Meloche, M. L. Plumer, and C. M. Pinciuc, *ibid.***76**, 214402 (2007).

[35] A. Rebei and G. J. Parker, Phys. Rev. B **67**, 104434 (2003).

[36] R. P. Erickson and D. L. Mills, Phys. Rev. B **43**, 10715 (1991).

[37] R. P. Erickson and D. L. Mills, Phys. Rev. B **44**, 11825 (1991).

[38] H. Suhl, *Relaxation Processes in Micromagnetics* (Oxford University Press, New York, 2007).

[39] Y. S. Gui, A. Wirthmann, and C.-M. Hu, Phys. Rev. B **80**, 060402(R) (2009); **80**, 184422 (2009).

[40] Y. Khivintsev, J. Marsh, V. Zagorodnii, I. Harward, J. Lovejoy, P. Krivosik, R. E. Camley, and Z. Celinski, Appl. Phys. Lett. **98**, 042505 (2011).

[41] M. Krech, A. Bunker, and D. P. Landau, Comput. Phys. Commun. **111**, 1 (1998).

[42] P. B. Visscher and X. Feng, Phys. Rev. B **65**, 104412 (2002).